

# A Pseudo OFDM With Miniaturized FSK Demodulation Body-Coupled Communication Transceiver for Binaural Hearing Aids in 65 nm CMOS

Wala Saadeh, *Member, IEEE*, Muhammad Awais Bin Altaf, *Member, IEEE*,  
Haneen Alsuradi, *Student Member, IEEE*, and Jerald Yoo, *Senior Member, IEEE*

**Abstract**—A power-efficient body-coupled communication pseudo orthogonal frequency-division multiplexing (P-OFDM) transceiver (TRX) is presented for binaural hearing aids (BHAs). Channel measurements are performed for different body postures between human head-to-hand and ear-to-ear to characterize the body channel path loss. The TRX exploits baseband 16-quadrature amplitude modulation OFDM symbols transmitted through a binary frequency-shift keying (FSK) modulation to mitigate the multipath and interference problems, which are the most serious issues in BHA, with bit error rate improvement of 74% compared to FSK. It is also free from the peak-to-average power ratio problem. A power-of-two decomposition constant multiplier is implemented to achieve area-efficient constant multiplications in 64-FFT. The proposed energy- and area-efficient miniaturized direct conversion FSK demodulation receiver is capable of demodulating up to 20 Mbps signals while reducing the area by >50% compared to conventional implementations. The 1 Mbps TRX is implemented in a 65 nm CMOS process with an active area of 2.13 mm<sup>2</sup> while consuming 1.4 mW.

**Index Terms**—Adaptive frequency hopping (AFH), body area network, body-coupled communication (BCC), binaural hearing aids (BHAs), pseudo-orthogonal frequency-division multiplexing (P-OFDM), frequency-shift keying (FSK), peak-to-average power ratio (PAPR).

## I. INTRODUCTION

MORE than 5% of the world's population and ~33% of people aged above 65 suffer from hearing loss [1], which is becoming a serious social and health issue. It impacts information exchange and affects everyday life [2]. At a young age, hearing loss can also impede language acquisition.

Manuscript received June 13, 2016; revised September 16, 2016 and November 10, 2016; accepted December 2, 2016. Date of publication January 24, 2017; date of current version March 3, 2017. This work was funded by the Semiconductor Research Corporation (SRC) under the ATIC-SRC Center of Excellence for Energy Efficient Electronics Systems (ACE4S) Task 2440.008. This paper was approved by Associate Editor Waleed Khalil.

W. Saadeh and M. A. B. Altaf were with the Department of Electrical Engineering and Computer Science, Masdar Institute of Science and Technology, Abu Dhabi, UAE. They are now with the Electrical Engineering Department, Lahore University of Management Sciences, Lahore 54792, Pakistan.

H. Alsuradi is with the Department of Electrical Engineering and Computer Science, Masdar Institute of Science and Technology, Abu Dhabi 54224, United Arab Emirates.

J. Yoo was with the Department of Electrical Engineering and Computer Science, Masdar Institute of Science and Technology, Abu Dhabi, United Arab Emirates. He is now with the Department of Electrical and Computer Engineering, National University of Singapore, Singapore 117583 (e-mail: jyoo@nus.edu.sg).

Color versions of one or more of the figures in this paper are available online at <http://ieeexplore.ieee.org>.

Digital Object Identifier 10.1109/JSSC.2016.2639536

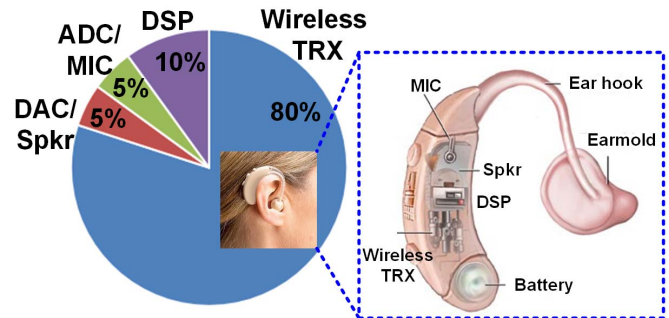


Fig. 1. BHAs application structure and power distribution [12].

Wearable electronics such as binaural hearing aids (BHAs) help individuals suffering from hearing loss to obtain more natural hearing [3], [4]. Binaural hearing permits the brain to receive the information necessary to filter out unwanted noise, to recognize one voice in a mixture of voices, or to identify the direction of signals where they are coming from [4]–[6]. Two hearing aids allow a greater benefit of directionality, as it incorporates a network of four microphones across them [7]. An essential requirement for a BHA device is to communicate between the two hearing aids to: 1) stream audio signals and 2) exchange useful commands for multiple purposes such as synchronization and volume control functions [8]. The ability to stream an audio signal between hearing aids enables more advanced beamformed responses compared to a single hearing aid [7].

Recently, short range and high data rates wireless communications such as wireless personal and body-area networks are widely used for battery-powered devices [9], [10]. Since these applications are powered by a battery, low power consumption is one of the key design challenges. Fig. 1 shows the structure of a BHA and its distribution of power consumption, where the wireless transceiver (TRX) for communication between the two ears consumes 80% of the total power of the device [11]. Existing wireless standards such as Bluetooth, ZigBee, and RFID may provide connectivity for this application, but they have several problems such as low data rate, large power consumption [11], [13], and most problematically, suffer from body shadowing [14]–[17]. Body shadowing effect can lead to more than 20 dB of attenuation with the small antennas placed near to the human body adding additional 10–15 dB of attenuation [10], [14]. Fig. 2 shows the relative relation

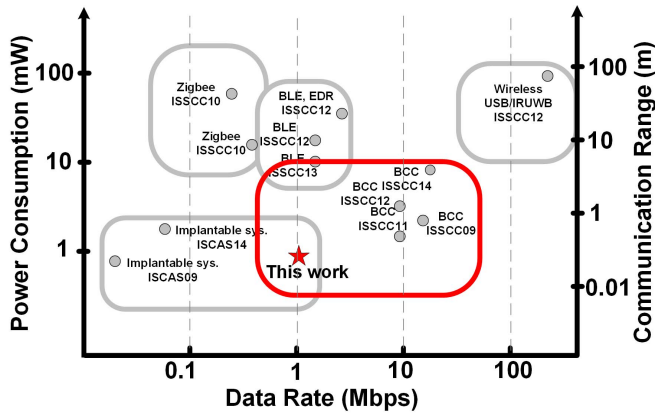


Fig. 2. Communication distance versus data rate and power consumption of wireless standards.

between the communication distance, data rate, and power consumption of the state-of-the-art TRXs [18].

To overcome such obstacles of communicating in close vicinity to the human body, body-coupled communication (BCC) can be utilized for an energy efficient implementation with acceptable data rate and communication distance [19], [20]. The BCC uses the human body itself as a communication medium, so it does not suffer from body shadowing, and enables efficient and reliable data communication between nodes in contact with or in close proximity to the human body [19]. Reference [21] presents a BCC TRX utilizing skin conductance designed for BHA, but with an optimistic channel path loss measurement, since it assumes a firm and stable ground connection. Noting that the return path in BCC is based on the parasitic ground, the ground connection is always dynamically changing. Therefore, the signal may have multiple return paths based on the capacitive coupling with the earth ground [22]. In addition, the signal may also have multiple forward paths due to different body compositions (i.e., fat, muscles, and bones), each of which has a different conductivity [23], [24]. This allows the transmitted signal to follow different paths depending on the on-body location of both TX and RX and the length of the transmission channel. Therefore, the ear-to-ear link is also affected by signal multipath fading problem [25]. Other nearby TRXs communicating in the BCC frequency range such as the FM radio and walkie-talkie will also interfere with the desired signal and can degrade the signal-to-interference ratio of BCC, which will impede the bit error rate (BER) performance. No work has been reported in the literature to mitigate these main channel impairments in the ear-to-ear link at once [26], [27]. This paper addresses the interference and signal multipath fading problems with minimum area and power consumption in BCC. The proposed pseudo-orthogonal frequency-division multiplexing (P-OFDM) TRX overcomes these issues by utilizing a baseband OFDM modulated into two main carriers using binary frequency-shift keying (FSK) modulation [28]. The baseband OFDM with cyclic prefix solves the multipath issue and mitigates the effect of the interference compared with normal FSK modulation

TRXs.

The OFDM signal has intermittent large peaks and small average value in its power, which makes the peak-to-average power ratio (PAPR) high. Due to limited dynamic range of the digital-to-analog converters (DACs) and limited linear range of the power amplifier (PA), the conventional OFDM suffers from high PAPR, which requires additional methods to mitigate the issue. Such techniques complicate the design or introduce more BER. On the other hand, the proposed P-OFDM TRX eliminates the extra overhead of the two analog-to-digital converters (ADCs), two DACs, and PA used in the conventional OFDM TRXs; as a result, power and area usage are reduced by 67% and 59%, respectively [28]. In addition, the proposed system is free from the PAPR problem, which is the major drawback in the OFDM-based system, because both DACs and PA are eliminated from this design. A variable-gain low-noise amplifier (LNA) and adaptive frequency hopping (AFH) technique are also exploited to ensure reliable and robust communication. FSK modulation carries the information in terms of frequency, which makes it more robust against amplitude distortion [29]. FSK modulation can be easily implemented based on direct switching from phase-locked loop (PLL) output. However, FSK demodulation can be a challenging task. The proposed miniaturized direct conversion receiver (RX) simplifies the demodulation process and reduces power consumption.

This paper is organized as follows. Section II describes the body channel measurement that discusses the path loss behavior of the ear-to-ear body channel. Section III explains the proposed P-OFDM TRX structure. Section IV shows the P-OFDM symbol generation and recovery implementation, and Section V describes the proposed miniaturized direct conversion FSK demodulation RX. The measurement and verification results are described in Section VI. Finally, Section VII concludes this paper.

## II. CHANNEL PATH LOSS MEASUREMENTS

In order to estimate the body channel path loss, a channel measurement is conducted between human head-to-hand and ear-to-ear. It is performed with a sitting posture of the human subject with 0 dBm transmitter (TX) power which is below the safety limit of (0.08 W/kg) in the frequency range below 10 GHz [30]. In the capacitive coupled BCC, the signal return path is constructed from the capacitive coupling between the human body (floating ground electrodes of both TX and RX) and the earth ground (the floor where the person is standing). The relative position of the TX/RX from the earth ground, the location of TX/RX and movements will cause variations in the coupling strength and therefore affect the channel characteristics [32]. Fig. 3 shows the measurement setup, where an RF generator is used as TX with variable frequency of transmission. A spectrum analyzer is used to detect the signal and balanced-to-unbalanced (Balun) is utilized for ground isolation in order to reflect the real scenario of floating ground electrodes [31].

Fig. 4(a) shows the channel path loss measurement results for 5 cm distance of communication on an arm for

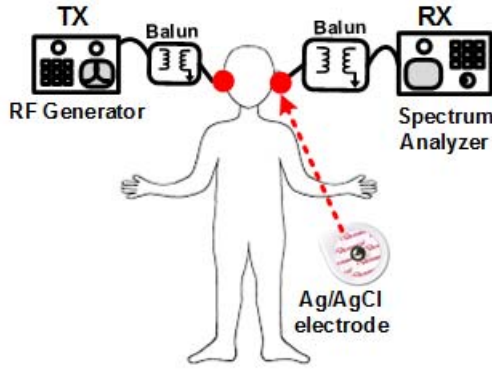


Fig. 3. Channel measurement setup for path loss estimation.

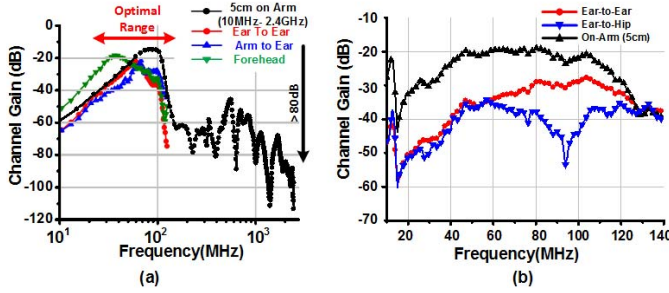


Fig. 4. Channel path loss characteristics measurement for different communication points on the human body for frequency range (a) (10 MHz–2.4 GHz) log scale and (b) 10–140 MHz.

the 1 MHz–2.4 GHz range on log scale. The results indicate a significant path loss with  $>80$  dB of attenuation around GHz's range within the vicinity of the human body, which proves that the conventional RF utilizing 2.4 GHz center frequency (ZigBee, Bluetooth, etc.) are not optimal for wearable communication; unless Line-of-Sight is guaranteed, the RF TRX will experience a huge path loss. The channel path loss measurements for ear-to-ear, ear-to-arm, and ear-to-hip communication channels are also shown in Fig. 4(b) in the frequency range (10–140 MHz). By changing the transmission and reception locations, the channel gain will be affected [32]. Frequency selective fading is observed for long communication distances [33]. For communication between the two ears, the optimal frequency range is between 20–100 MHz as shown in Fig. 4 [31]. Thus, in this work, a 4 channels (bandwidth of 40 MHz for each channel) AFH technique that covers the frequency range of 20–120 MHz is utilized for interference resilient transmission for BHAs [27], [29]. The last channel (80–120 MHz) will be used only if the initial three channels are not available.

### III. PROPOSED P-OFDM TRANSCEIVER ARCHITECTURE

OFDM transmission depends on dividing a high data rate signal into a multiple lower data rate streams that are transmitted over a number of subcarriers at the same time. It is mainly used in channels with multipath fading characteristics in order to mitigate the frequency selectivity and avoid intersymbol interference (ISI). The OFDM systems utilize pilot subcarriers and cyclic prefix (CP) that is appended to OFDM symbol to overcome the multipath channel reflections and reduce ISI by

simplifying channel estimation and equalization process. A CP is a copy of the last portion of the OFDM symbol that is added at the beginning of the symbol. The main advantage of the CP is that it causes the multipath replicas of the original signal to fade and prevent them from interfering with the adjacent symbols and introducing ISI. The transmitted OFDM signals can have high peak values in the time domain since multiple subcarrier components are added through an Inverse Fast Fourier Transformation operation. As a result, OFDM systems are known to have a high PAPR when compared with single-carrier systems. In fact, the high PAPR is one of the most critical problems in an OFDM system as it reduces the signal-to-quantization noise ratio of the DACs and ADCs and degrades the efficiency of the PA. Clipping those large peaks will introduce in-band distortion (high BER) and out-of-band radiation into the channel.

This paper introduces the P-OFDM modulation method, which is based on transmitting baseband OFDM symbols via AFH based FSK modulation to mitigate signal multipath and interference problems compared to having only a binary FSK modulation [28]. In the P-OFDM modulation, the physical layer transmission is through binary FSK and not the OFDM itself. However, the baseband OFDM symbols act as a pre-coded signal passed to the FSK modulation. The advantage of transmitting the OFDM symbols compared to original input data bits is that the OFDM symbols require FFT/IFFT operation that involves frequency domain operation. Therefore, the channel estimation will occur in the frequency domain in P-OFDM, which significantly simplify the channel estimation and equalization operations compared to having FSK modulation with time domain equalization. The proposed P-OFDM modulation can be also considered as a new form of single carrier modulation with frequency domain equalization [32], [35]. The channel equalization is implemented in the frequency domain using decision feedback equalizer (DFE) [32]. This significantly reduces the complexity of the equalizer implementation and provides superior performance compared to time domain equalization [36], [37]. By combining FFT processing and the CP, the single carrier system with frequency domain equalization has essentially the same performance as an OFDM system with low complexity [38], [39]. At the RX side, the received OFDM symbol including CP and pilot subcarriers are utilized to perform synchronization, channel estimation and training functions. If significant attenuation is encountered, a resend signal will also be set to high. This is an advantage of OFDM systems due to the inherited nature of channel estimation gained from the pre-known pilot subcarriers and CP [32]. Therefore, P-OFDM helps in mitigating the signal multipath and the interference issues compared to FSK-only modulation. The assumption here is that no equalization is used in the case of using FSK-only modulation. In the P-OFDM, the effective energy per bit will be [40]

$$\bar{E}_b = \frac{1}{M} \cdot \sqrt{\frac{R}{2}} \cdot E_b \quad (1)$$

where  $R$  is the number of bits for representing the OFDM symbol in the P-OFDM and  $M$  is the number of constellation points used in the P-OFDM.  $E_b$  is the signal energy associated



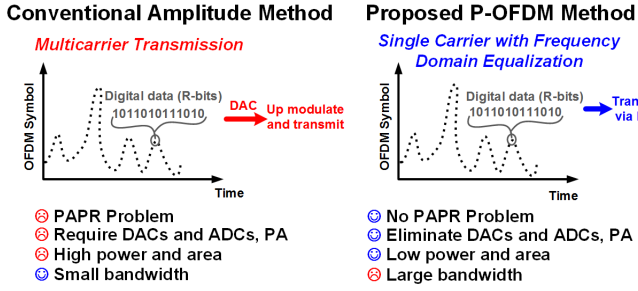


Fig. 5. Comparison between the proposed modulation versus conventional approach.

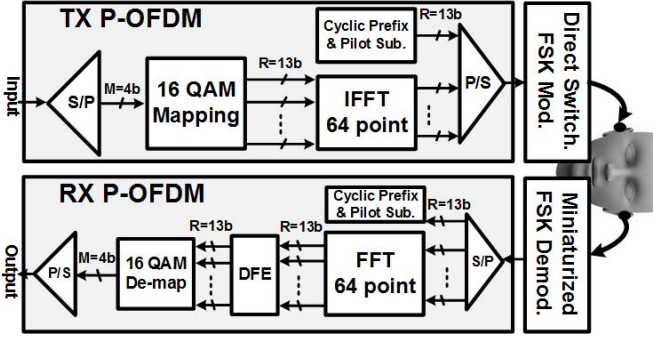


Fig. 6. Proposed P-OFDM TRX block diagram.

with each data bit. Therefore, the BER can be expressed as

$$BER_{P-OFDM} = \frac{1}{2} \operatorname{erfc} \left( \sqrt{\frac{1}{M} \cdot \sqrt{\frac{R}{2}} \cdot \frac{E_b}{2N_0}} \right). \quad (2)$$

$E_b/N_0$  is the energy per bit to noise power spectral density (PSD) ratio. It can be realized the  $BER_{P-OFDM}$  is much lower compared to  $BER_{FSK}$  [40] and [41].

In the P-OFDM, the same baseband OFDM symbol is being sent but through the FSK modulation with sufficient bandwidth to accommodate the symbol bits and avoid ISI. The OFDM symbol is maintained to be in the digital domain (i.e., not converted to analog using DAC) and the symbol bits are being transmitted using FSK modulation. This effectively eliminates the need for the two ADCs, two DACs and PA employed in the conventional OFDM TRXs. In addition, it will be free from the PAPR problem caused by the nonlinearity of DACs and PA as both of them will be eliminated from the system. Fig. 5 explains the difference between the proposed P-OFDM method which is a single carrier frequency with frequency domain equalization and the conventional multicarrier amplitude-based OFDM. In the conventional OFDM, the OFDM symbol (R-bits) is converted to analog using DAC and then forwarded for up modulation while in P-OFDM these R-bits are directly transmitted with the FSK. Fig. 6 shows the block diagram of the proposed system where the input data is grouped into lower data rate streams that are transmitted concurrently over 64 subcarriers. A 16-quadrature amplitude modulation (QAM) constellation with 64 subcarriers are used in order to generate the different constellation points and achieve a data rate transmission of 1 Mbps.

The incoming data stream (1 Mbps) is classified into 4 b, which are used by the 16-QAM mapping block to generate 13 b (I, Q) constellation points for each subcarrier input of the 64-point IFFT. The time required to generate each subcarrier input is  $4 \mu s$  and in order to generate the full 64 input set, 32 of such inputs (total duration of  $128 \mu s$ ) are essential to consist the input set of the IFFT while the rest 32 will be set to zero to simplify the computations. The IFFT block in the TX side is used to modulate these constellation points. After that, the CP, which is a copy of last 16 IFFT output subcarriers and 16 pilot subcarriers, are appended to help synchronization and channel estimation. Each of these subcarriers' output is composed of 26 bits (13 imaginary and 13 real). Then the output bits are streamed and passed into a direct switching binary FSK modulator. Therefore, the resultant data rate of FSK TX/RX is  $\sim 20$  Mbps. In the FSK modulation, the channel quality is checked to identify a clean channel free from interference for transmission using AFH technique. On the RX side, the signal is first demodulated using the proposed miniaturized Direct Conversion FSK demodulator and then CP is disregarded. The data stream is then forwarded to fast Fourier transform (FFT) block and then to the DFE for channel estimation using the pilot subcarriers and finally demodulate the transmitted bits through a 16-QAM de-mapping block to generate the original message bits.

#### IV. P-OFDM SYMBOL GENERATION AND RECOVERY

In the OFDM system, the IFFT and FFT pair are utilized to modulate and demodulate the transmitted data constellation on the subcarriers. The FFT/IFF functions are derived from the main function, namely Discrete Fourier Transform (DFT/IDFT); using FFT/IFFT instead of DFT/IDFT leads to faster computation and a reduced number of calculations. For the FFT/IFFT, the conventional Cooley–Tukey radix-2 FFT algorithm requires 192 complex butterfly operations, for a 64-point FFT computation. A radix-2 butterfly unit requires one complex multiplication and two complex additions. In addition to butterfly unit, a memory unit is required to store the complex twiddle factors and complex intermediate data, which complicates addressing logic and control circuitry as well as requires more area. FFT function of length  $N$  can be realized by first decomposing it into one  $M$  and one  $T$ -point FFT where  $N = M \cdot T$ , and then combining them as shown in (3). This essentially results in a 2-D structure instead of a 1-D structure of FFT [42]

$$A(c+Tt) = \sum_{r=0}^{M-1} W_M^{rt} \left[ W_{M \cdot T}^{cr} \sum_{m=0}^{T-1} B(r+Mm) W_T^{cm} \right] \quad (3)$$

where  $A$  and  $B$  represent the complex output and input data, respectively. The variables  $r$  and  $c \in \{0, 1, \dots, T-1\}$ ,  $t$  and  $m \in \{0, 1, \dots, T-1\}$ , and the  $W_{M \cdot T}^{cr}$  represent the 2-D constants or twiddle factors as

$$\text{Twiddle Factors}(W_{M \cdot T}^{cr}) = e^{\frac{-j2\pi cr}{M \cdot T}}. \quad (4)$$

The 64-point FFT/IFFT block is implemented by decomposing it into a 2-D structure of 8-point FFTs plus 64 complex

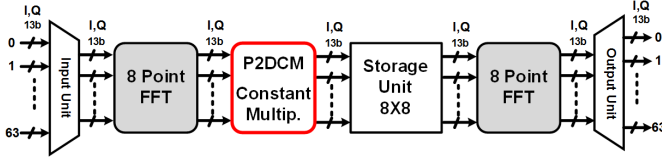


Fig. 7. Sixty-four-point FFT/IFFT block diagram.

2-D constant multiplications as expressed in (5) by setting both  $M$  and  $T$  to 8 [42]

$$A(c+8t) = \sum_{r=0}^7 \left[ W_{64}^{cr} \sum_{m=0}^7 B(r+8m) W_8^{cm} \right] W_8^{rt} \quad (5)$$

where the variables  $r, c, t$ , and  $m \in \{0, 1, \dots, 7\}$ . This approach reduces the number of required complex multiplications to only 64. Both the FFT and IFFT can be implemented using the same hardware by exchanging the real and imaginary parts of the incoming data at the input, and exchanging the real and imaginary parts of the data back at the output. Fig. 7 shows the block diagram of the 64-point FFT/IFFT implementation. The incoming input data go through an 8-point FFT computation according to the correct order followed by eight parallel constant multiplications with the  $(W_{64}^{cr})$ . The results are stored into a  $13b \times 8$  2-D storage unit. Eight such computations are needed to generate a full set of 64 intermediate data, which once again go through a second 8-point FFT in order. In this implementation, the output data are generated in the correct order and no rearrangement of the data is required at the output unit compared to the design in [42]. The implemented FFT/IFFT block performs the full 64-point FFT in 16 clock cycles versus 23 clock cycles in [32] because of the proposed power-of-two decomposition constant multiplier (P2DCM). Each 8-point FFT function is implemented using the decimation in time butterfly algorithm without using any explicit multiplication operation. From (5), it can be realized that complex floating-point (FP) multiplication with constants is required. These constants FP multiplication are a bottleneck in the implementation of an area-and-energy efficient 64-point FFT. The proposed implementation reduces area-and-energy consumption of overall 64-point by  $>90\%$ , compared to the conventional 64-point FFT implementation in [37].

The proposed P2DCM utilizes the IEEE Standard for FP Arithmetic (IEEE 754) in custom format by exploiting 13 b as shown in Fig. 8. The 13 b FP number contains three parts: a single sign bit, an exponent part (5 b), and a fraction part (7 b). The 64-point FFT is limited by area, and if we adopt conventional implementation [43], the resources consumed by the FP multiplier will reach  $\geq 65\%$  of the total chip area; this is due to conventional multipliers, which take a significant portion. The proposed P2DCM utilizes 21K logic gates compared to 68 K of conventional FP multiplier [43] for 13 b precision. In the IEEE 754 FP format, the multiplication and division of any number translate into simple addition and subtraction if the multiplicand is in the power of 2. In the proposed 64-point FFT implementation the constants are known *a priori*, and to exploit this feature, the constants are decomposed into  $2^n$ , as shown in Fig. 8. The example in

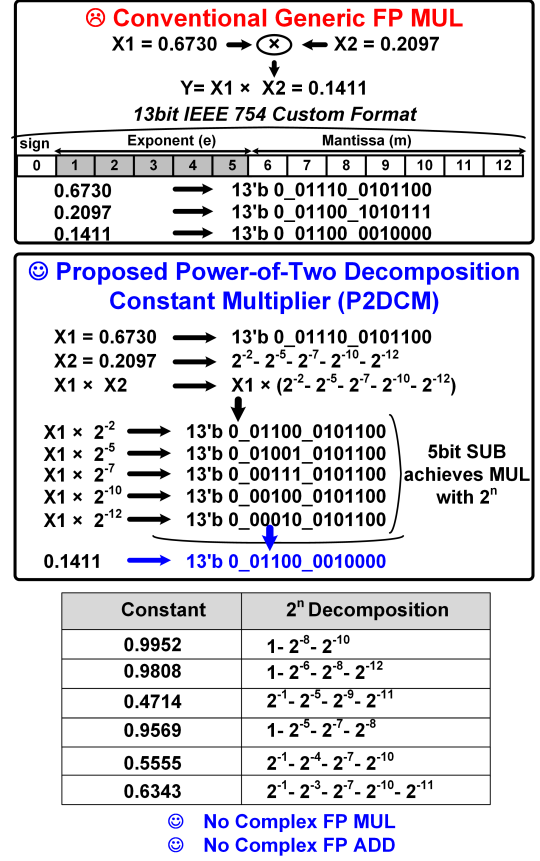


Fig. 8. Proposed P2DCM.

the diagram shows the multiplication of two FP numbers with just simple addition and subtraction operation. The number  $X1$  is an incoming multiplicand, whereas  $X2$  is a known constant, which is decomposed into  $2^n$ . P2DCM does not require any FP multiplication and/or complex FP addition or subtraction operation. Some constants' decompositions into  $2^n$  are also shown in the table in the diagram. Fig. 9 shows the hardware implementation of the proposed P2DCM for a specific constant with value 0.2097. Based on the decomposition into  $2^n$  of constant, the mantissa part of incoming input are compared to corresponding "n" using a 5 b comparator. The purpose of the comparator is to decide the input value level to avoid any false data computation. If the incoming mantissa value is less than compared "n", then zero value is passed as mantissa to the add/subtract unit. The selection between the subtracted and zero mantissa is controlled by the comparator and processed by the multiplexer. The implementation of 5 b comparator is achieved using an area-efficient very simple couple of gate (VSCG) architecture as shown in Fig. 9 due to the presumptive compared value. As an example, comparing with '2' requires only two OR gates and one AND gate. The VSCG reduces the number of logic gates by more than 80–90% compared to the conventional 5 b comparator.

## V. PROPOSED MINIATURIZED DIRECT CONVERSION FSK DEMODULATION

FSK signal can be demodulated asynchronously, using envelope detectors. However, this is inappropriate for the BCC

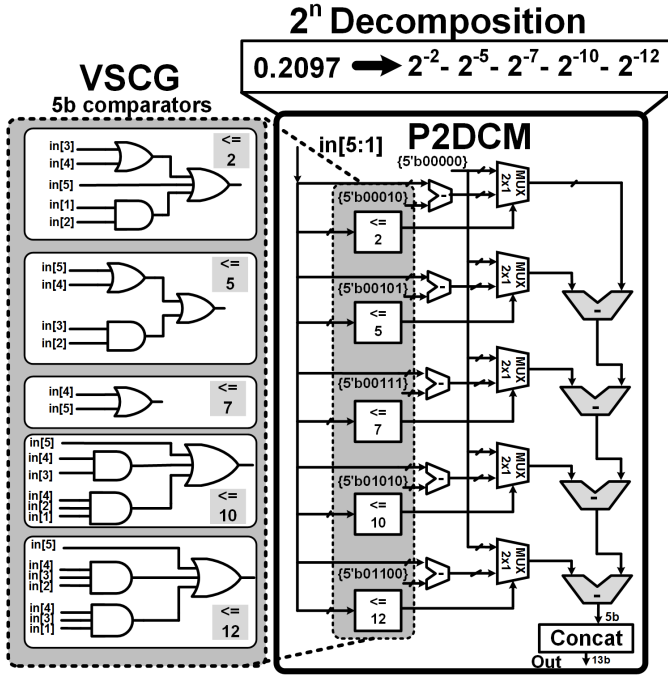


Fig. 9. Constants multiplication implementation.

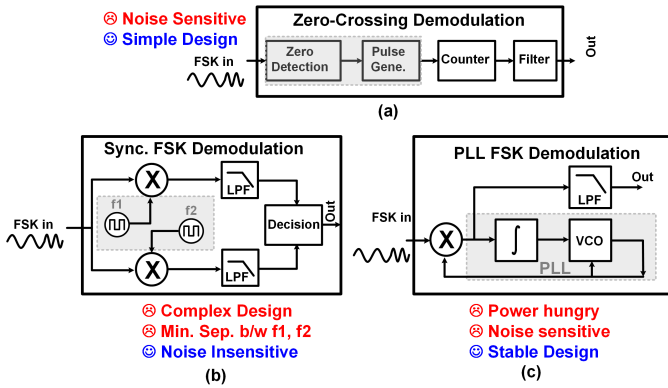


Fig. 10. Conventional FSK demodulation techniques. (a) Zero-crossing method. (b) Synchronous method. (c) PLL-based method.

since the channel path loss is not fixed across all frequencies, which make the detection based on amplitude not reliable. Fig. 10 shows three different conventional types of FSK demodulation. In Fig. 10(a), a zero-crossing demodulator is shown, which works on the principle that the information in the signal, contained in the local frequency of the signal, is equal to the inverse of the period of the signal. Therefore, the period of the signal is measured by checking the zero crossing to determine its local frequency. The zero-crossing demodulator is area efficient for an on-chip implementation but due to the interference and the multipath fading in the modulated BCC signal, it is not preferred in the current implementation. Fig. 10(b) shows a synchronous FSK demodulator where two local carriers, on each of the two frequencies of the binary FSK signal, are used in two synchronous demodulators. A decision circuit checks the two outputs and decides the output bit. A PLL is another well-known method of demodulating an FSK signal as shown in Fig. 10(c). The PLL has

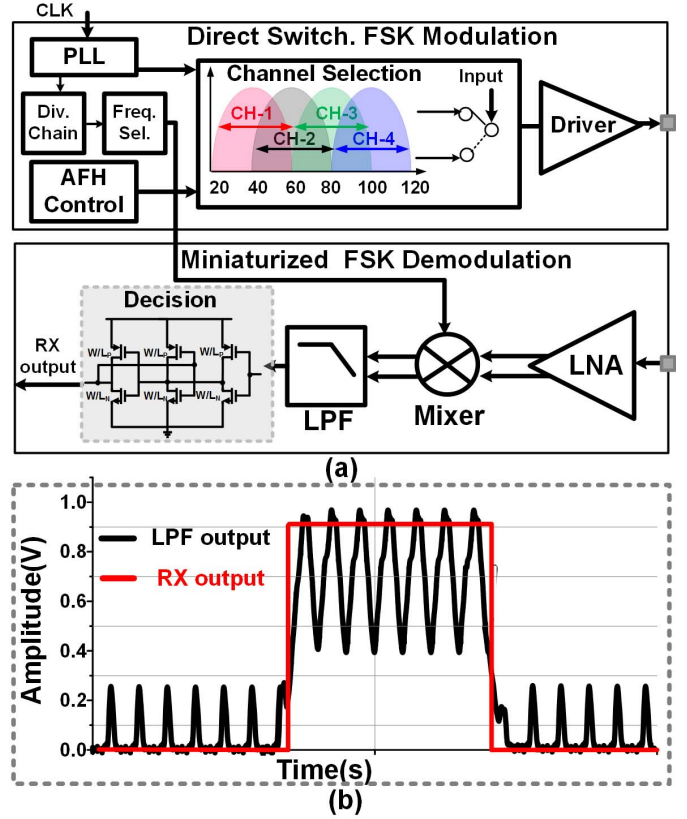


Fig. 11. (a) FSK TRX block diagram with proposed miniaturized zero-IF FSK demodulation RX architecture. (b) Measurements of the LPF and RX outputs.

a phase detector on the front end that takes two inputs. One input is the feedback, the other is the incoming signal. The reference frequency is controlled by the voltage controlled oscillator (VCO). Since it is a closed-loop system, the feedback path will adjust the VCO to match the incoming signal. If the incoming signal shifts in frequency, the voltage to the VCO will change to match. Based on the bandwidth of the loop integrator, a separate low-pass filter (LPF) is required to recover the original message.

Fig. 11(a) shows FSK modulation and demodulation blocks in the proposed P-OFDM BCC TRX with the block diagram of the proposed miniaturized direct conversion FSK demodulation RX. The AFH control block performs AFH algorithm scheme to hop between the four channels and the channel selector performs direct switching FSK modulation. In the proposed implementation, the two frequencies of the binary FSK are equally distanced (20 MHz) from the LOs carrier frequency for each channel. On the RX side, the incoming FSK modulated signal is first amplified with a gain of 15–27 dB by the reconfigurable gain LNA to compensate for the losses induced by the channel. Then, the amplified FSK modulated signal is downconverted to baseband (20 MHz in this implementation) using a Gilbert cell mixer with out-of-phase clock signals to eliminate any nonlinearity caused by both inputs ( $V_{in+}$ ,  $V_{in-}$ ) mixing simultaneously. Since the two frequencies of the FSK are equally distanced from the LO's frequency, by demodulating the FSK signal using a single mixer, it will

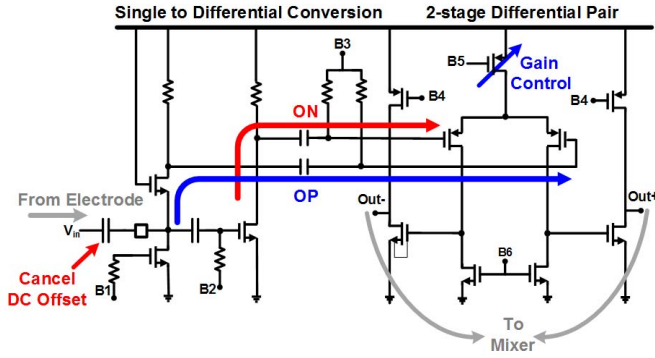


Fig. 12. Schematic of three-stage single to differential LNA.

be transformed to 20 MHz. After that, an LPF with a cutoff frequency of 25 MHz will reject unwanted high frequency signals generated after the mixing operation. Finally, the output of the LPF of 20 MHz frequency represents the received bits but they are not clean pulses as shown in Fig. 11(b). Therefore, a decision circuit based on a Schmitt trigger hysteresis is used to decide the received signal bit correctly (bit 0 or bit 1). The functionality of the proposed demodulation method is tested against all process corners to verify that PVT variations do not affect the performance. The proposed RX overcomes the major limitations of the conventional FSK demodulation approaches. It eliminates the need for power hungry PLL/DLL and allows for synchronous detection with a simple implementation which reduces the power consumption and area by >50% compared to [26] and [29].

The RX input coming from the electrode is single ended in nature. On the other hand, differential signals in the RX chain are preferred in order to reduce second-order distortion and to reject power supply and substrate noise. Thus, in the RX chain, a Balun is required to convert the single-ended input signal into a differential signal. In this RX implementation, a single ended-to-balanced differential conversion LNA is utilized for generating a differential input signal for the mixer. Fig. 12 shows the proposed three-stage LNA schematic with single to differential conversion implemented. The common-gate (CG) followed by common source (CS) amplifiers provides the conversion required. The CG outputs the in-phase, whereas the CS inverts the input signal. The gain of the CG and CS is designed to be the same but with a 180° phase difference. This scheme eliminates the need for external Balun as a single to a balanced output converter. In addition, it offers a noise cancellation scheme inherited in this structure [44]. The functionality of the proposed LNA design is tested against all the process corners to verify that PVT variations do not affect the performance. The third stage is added to increase the gain as well as limiting the LNA bandwidth to 120 MHz. It eliminates the need for additional LPF with 120 MHz cutoff frequency placed at the input of the LNA to reject out-of-band signals and noise. The LNA offers variable gains of (15, 21, 23, and 27 dB) with bandwidth from 20 to 120 MHz to reject out of band noise. The implemented LNA reduces the area by 42% compared to [45]. A multiple feedback (MFB) second-

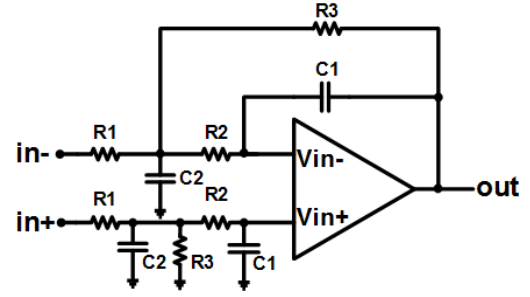


Fig. 13. Schematic of MFB second-order LPF.

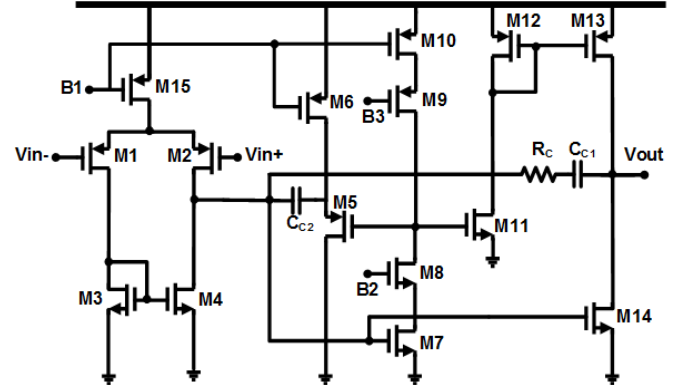


Fig. 14. Schematic of the implemented three-stage amplifier.

order LPF is implemented to provide 25 MHz cutoff frequency and convert the differential input into a single ended output at the same time. The MFB circuit shown in Fig. 13 is a second-order low-pass stage that can be used to realize one complex-pole pair in the transfer function of an LPF given as

$$H(s) = -\frac{\frac{R2}{R1}}{(R2R3C1C2)s^2 + (R2+R3+\frac{R2R3}{R1})C1s+1}. \quad (6)$$

The implementation of an LPF requires a high gain and bandwidth amplifier. The design of this amplifier is challenging, as it is required to have a unity gain frequency much higher than the cutoff frequency of the LPF. In the proposed amplifier implementation, a frequency compensation scheme for three-stage operational transconductance amplifiers, namely, the reversed nested Miller compensation (RNMC) is utilized [46]. The simplified schematic of the implemented three-stage amplifier compensated using the RNMC technique is shown in Fig. 14. The compensation is realized through the Miller capacitors  $C_{C1}$  and  $C_{C2}$ , the resistor  $R_C$ , and the inverting feedforward stage  $gm_f$ . In this implementation and to achieve the desired bandwidth, the Miller capacitors  $C_{C1}$ ,  $C_{C2}$  and the resistor  $R_C$  are selected as 63 fF, 240 fF, and 1 KΩ, respectively. The first stage is realized by the PMOS differential pair (M1–M2) with a current mirror load (M3–M4). The feedforward stage  $gm_f$  is generated using the active load transistor M14 of the last stage, whose gate is connected to the output of the first stage. The second inverting stage is realized by cascode CS M7–M10, while the last noninverting stage is implemented by M11–M14. The cascode M7–M10 increases the gain and



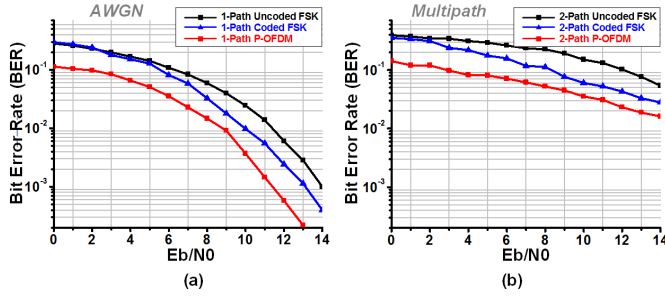


Fig. 15. Simulated BER performance versus SNR for uncoded FSK, coded FSK, and P-OFDM in channel modeled as (a) AWGN and (b) 2 paths channel.

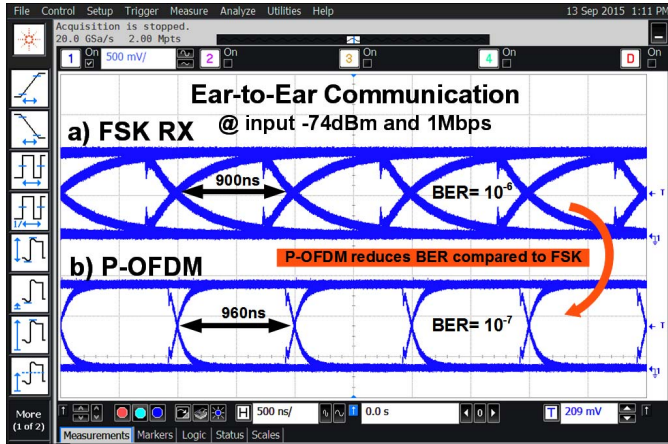


Fig. 16. Measured eye diagrams of the demodulated bit streams of (a) FSK and (b) P-OFDM modulations.

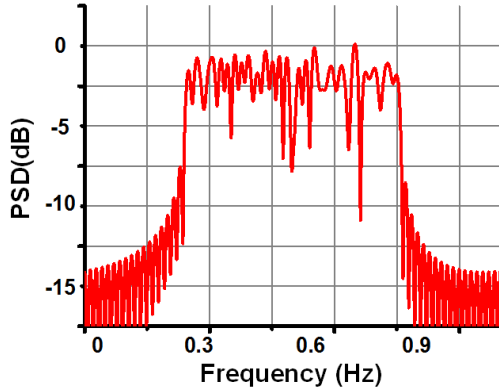


Fig. 17. Measured PSD of 64-point IFFT output.

unity gain frequency to  $>80$  dB and  $>100$  MHz, respectively, compared to [46] and [47].

## VI. IMPLEMENTATION RESULTS

The proposed P-OFDM TRX chip is implemented in 65 nm 1P7M CMOS process with 1.1 V supply voltage. In order to verify the superior performance of the P-OFDM, Fig. 15 shows the simulated BER performance of P-OFDM modulation, uncoded FSK, and coded FSK (Hamming (7-4)) versus channel quality represented by  $E_b/N_0$ , in no multipath and multipath channels. The P-OFDM system achieves  $\sim 74\%$  and  $\sim 53\%$

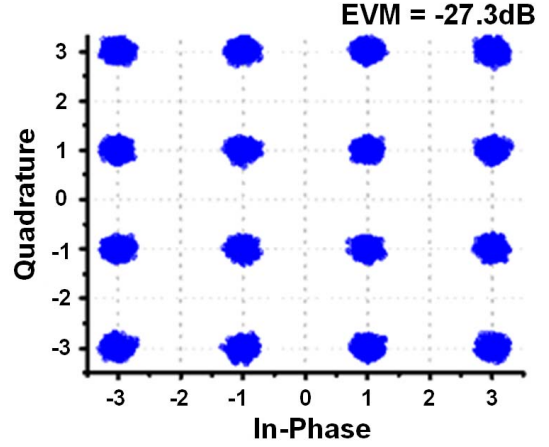


Fig. 18. Measured 16-QAM constellation points of the received bits.

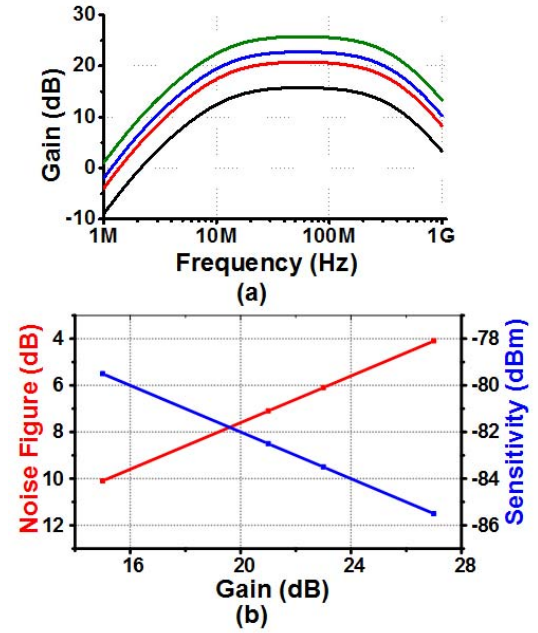


Fig. 19. LNA measurements. (a) Gain and bandwidth. (b) Noise figure and sensitivity.

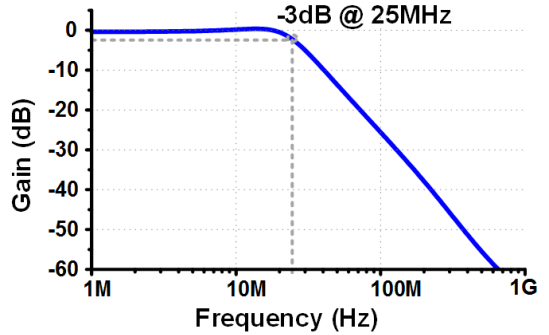


Fig. 20. Measured LPF gain-bandwidth characteristics.

reduction in BER compared to uncoded FSK and coded FSK, respectively. The inclusion of multipath here assumed a 2-path scenario where the second path has a 1 ns delay and  $-0.5$  dB attenuation. For the sake of comparing the performance of



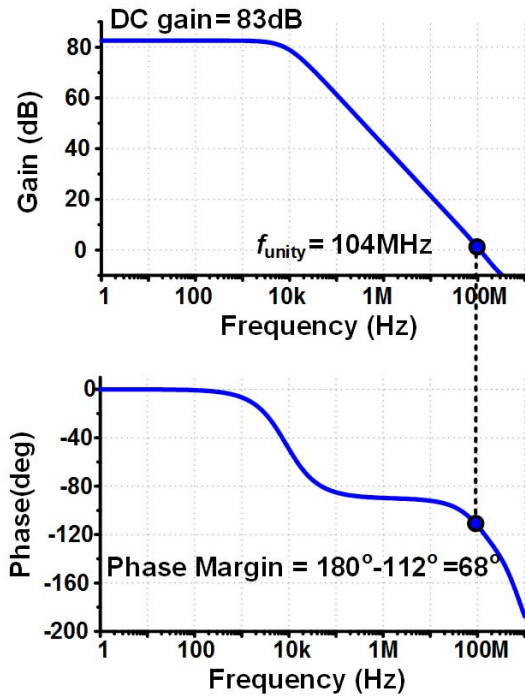


Fig. 21. Simulated RNMC amplifier performance. (a) Gain bandwidth. (b) Phase.

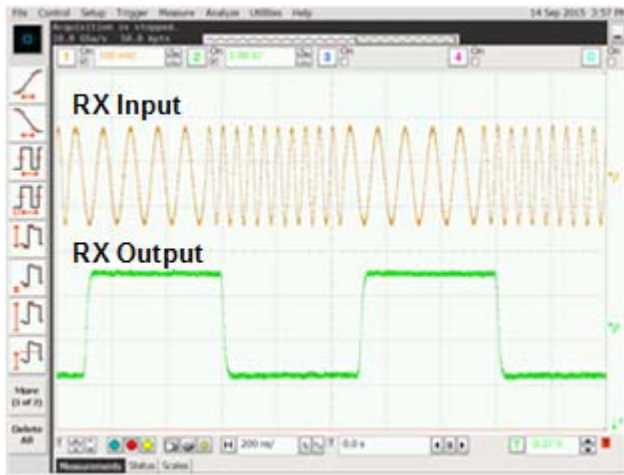


Fig. 22. Measured input and output of the FSK demodulation RX.

P-OFDM and FSK modulations, the measurements for the ear-to-ear channel are done on the full P-OFDM TRX and on the FSK TRX only with OFDM part is disconnected. The measured eye diagram at the  $-74$  dBm input power and 1 Mbps data rate of the demodulated bit streams on the RX side for ear-to-ear communication for both P-OFDM and FSK is shown in Fig. 16.

The top eye diagram (a) shows the result of the FSK TRX only (both P-OFDM TX and RX are disconnected) and it is measured at the FSK RX output. The bottom eye-diagram (b) shows the P-OFDM TRX result and it is measured at the P-OFDM RX output. The wider eye opening of P-OFDM (960 ns) compared to FSK TRX (900 ns) proofs for the better performance of P-OFDM for the ear-to-ear channel compared

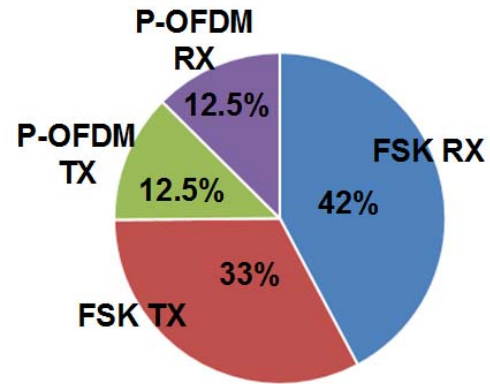


Fig. 23. Power distribution of the P-OFDM TRX.

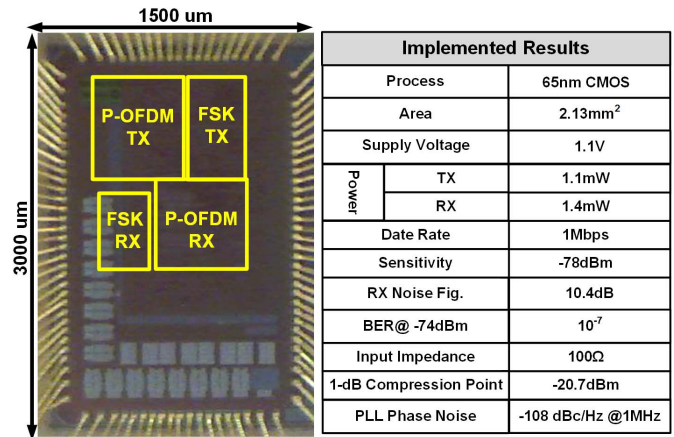


Fig. 24. Die photograph of the P-OFDM and performance summary.

to FSK. The measured BER of the P-OFDM TRX at an input of  $-74$  dBm is  $10^{-7}$  while the BER for the FSK is  $10^{-6}$ .

To understand the strength of the variations (energy) as a function of frequency, PSD of the orthogonal multicarrier output of the IFFT block is measured and plotted in Fig. 17. It shows power variations at different subcarrier frequencies with CP and pilot subcarriers frequencies, which corresponds to the output of 64 points IFFT shown in Fig. 7. It also verifies that the CP length of 16 subcarriers does not increase the variations at the generated ripples in the desired band and the subcarriers do not overlap each other at the subcarrier center frequencies, which guarantee no ISI and reduced BER. The measured constellation points for the 16-QAM demodulated bits with an error vector magnitude of  $-27.3$ dB is shown in Fig. 18. The full convergence of constellations in the correct quadrants of the IQ plane is achieved using the DFE, which can be verified from the large division instants between each constellation point. The random sequence length from PRBS generator is  $2^{12}$  b.

At the TX side, the driver provides an output power of  $-20$ – $0$  dBm based on the contact impedance of the TX-human body. While at the RX side, the LNA provides a variable gain to compensate for the losses induced by the body channel during signal transmission. Fig.19(a) shows the gain-bandwidth measurement results of LNA with variable gains

TABLE I  
COMPARISON WITH THE STATE-OF-THE-ART TRXS

	RF Technology			BCC			
Parameter	ISSCC 2012 [10]	ISSCC 2013 [13]	ISSCC 2014 [11]	JSSC 2012 [26]	ISSCC 2014 [27]	ISCAS 2015 [28]	This Work
Technology	90nm CMOS	90nm CMOS	65nm CMOS	180nm CMOS	65nm CMOS	65nm CMOS	65nm CMOS
Frequency Band	6-9GHz	2.4GHz	7.75-8.25GHz	40-120MHz	40-120MHz	20-120MHz	20-120MHz
PHY/Modulation	IR-UWB	QPSK	Chirp-UWB	Double FSK	3-Level Walsh	64 P-OFDM	64 P-OFDM + Mini. FSK DEM
Multipath Mitigation	X	X	X	X	X	O	O
Energy / bit	7.6nJ/b	9.2nJ/b	1nJ/b	0.24nJ/b	0.15nJ/b	1.54nJ/b	1.4nJ/b
Power Consumption	6.5mW	9.2mW	1mW PP : 7.5mW	2.4mW	9.02mW	1.54mW	1.4mW
Area	2mm <sup>2</sup>	2mm <sup>2</sup>	0.7mm <sup>2</sup>	12.5mm <sup>2</sup>	1.12mm <sup>2</sup>	2.28mm <sup>2</sup>	2.13mm <sup>2</sup>
Data Rate	0.85Mb/s	1Mb/s	1Mb/s	10Kb/s-10Mb/s	60Mb/s	1Mb/s	1Mb/s
BER	-	@-98dBm=10 <sup>-5</sup>	-	@-65dBm=10 <sup>-5</sup>	@-58dBm=10 <sup>-5</sup>	@-68dBm=10 <sup>-7</sup>	@-74dBm=10 <sup>-7</sup>
Sensitivity	-88dBm	-98dBm	-76dBm	-66dBm	-58dBm	-72dBm	-78dBm

\* PP = Peak Power

(15, 21, 23, and 27 dB). The noise figure and the sensitivity measurement for the different gain settings are also shown in Fig. 19(b). For weak input of the signal, the required gain is high with low noise figure and high sensitivity. The noise figure of LNA can be adjusted by changing the gain, from 4 to 10 dB, corresponding to a sensitivity of  $-85.5$  to  $-78$  dBm. The LNA also provides a bandpass bandwidth of 20–120 MHz (intended frequency of transmission), which will eliminate the need for an external bandpass filter to reject out-of-band noise signals. The measured LPF gain-bandwidth is shown in Fig. 20, which shows a cutoff frequency of 25 MHz, which will suppress the undesired high-frequency harmonics. The simulated gain-bandwidth and phase margin plots are shown in Fig. 21 for the high gain RNMC amplifier. It provides a dc gain of 83 dB and unity gain frequency of 104 MHz, which verifies its functionality to be utilized in the LPF operation while consuming 93  $\mu$ W. The demodulated output bits of the RX is measured to verify the functionality of the proposed miniaturized direct conversion FSK demodulation as shown in Fig. 22. The 20 Mbps RX is implemented in 65 nm CMOS process with an active area of 0.03 mm<sup>2</sup>, which is >50% lower area compared to the conventional implementation [29]. The measured RX sensitivity is  $-78$  dBm with a noise figure of 10.4 and 1-dB compression point of  $-20.7$  dBm. Fig. 23 shows the distribution of power consumption of the proposed P-OFDM TRX. It should be noted that 25% of the TRX is consumed by the OFDM symbol generation and recovery blocks. Fig. 24 shows the chip micrograph and the performance summary for the P-OFDM TRX with an active area of 2.13 mm<sup>2</sup>. Table I compares this TRX with the state-of-the-art works. References [26] and [27] provide energy-efficient TRXs but they do not provide a solution for the signal multipath issue of the BCC channel. The proposed TRX consumes 1.4 mW for the RX and 1.15 mW

for the TX while mitigating the signal multipath issue of the BCC.

## VII. CONCLUSION

The implemented 4-channel AFH P-OFDM BCC TRX overcomes the main channel impairments in BHA application. The proposed design is free from PAPR problem and eliminates DACs, ADCs, and PA from the conventional OFDM designs. The proposed P-OFDM TRX is implemented in a 65 nm 1P7M CMOS process with an active area of 2.13 mm<sup>2</sup>, having average BER improvement of 74% compared to FSK with a 1 Mbps data rate while consuming 1.4 mW. The proposed miniaturized FSK demodulation RX overcomes the limitations of conventional FSK demodulators. It eliminates the need for PLL/DLL and double branches in synchronous demodulation while reducing the area usage by >50% compared to conventional designs.

## REFERENCES

- [1] WHO. (2013). *Millions of People in the World Have Hearing Loss That Can be Treated or Prevented*. [Online]. Available: <http://www.who.int/pbd/deafness/news/Millionslivewithhearingloss.pdf>
- [2] A. Ciorba, C. Bianchini, S. Pelucchi, and A. Pastore, "The impact of hearing loss on the quality of life of elderly adults," *Clin. Intervent. Aging*, vol. 7, no. 6, pp. 159–163, Jun. 2012.
- [3] P. Avan, F. Giraudet, and B. Büki, "Importance of binaural hearing," *Audiol. Neurotol.*, vol. 20, no. 1, pp. 3–6, May 2015.
- [4] M. Boymans, S. Goverts, S. E. Kramer, J. M. Festen, and W. A. Dreschler, "A prospective multi-centre study of the benefits of bilateral hearing aids," *Ear Hearing*, vol. 29, no. 6, pp. 930–941, Dec. 2008.
- [5] H. J. Simon, "Bilateral amplification and sound localization: Then and now," *J. Rehabil. Res. Develop.*, vol. 42, no. 4, pp. 117–132, Aug. 2005.
- [6] L. Werner, *Human Auditory Development*. New York, NY, USA: Springer, 2011.

- [7] M. Latzel. (2012). Binaural voice stream technology—Intelligent binaural algorithms to improve speech understanding. Phonak Insight. [Online]. Available: <https://www.phonakpro.com/com/b2b/en/evidence/publications/phonak-insight.html>
- [8] Phonak Insight. (2013). *It's Sync or Stream, The Difference Between Wireless Hearing Aid Features and Binaural Voice Stream Technology*. [Online]. Available: [https://www.phonakpro.com/content/dam/phonak/gc\\_hq/b2b/en/elearning/publications/insight/2013/Insight\\_BVST\\_Nr3\\_The\\_two\\_Sides\\_of\\_Binaural\\_028-0890.pdf](https://www.phonakpro.com/content/dam/phonak/gc_hq/b2b/en/elearning/publications/insight/2013/Insight_BVST_Nr3_The_two_Sides_of_Binaural_028-0890.pdf)
- [9] M. Contaldo, B. Banerjee, D. Ruffieux, J. Chabloz, E. L. Roux, and C. C. Enz, "A 2.4-GHz BAW-based transceiver for wireless body area networks," *IEEE Trans. Biomed. Circuits Syst.*, vol. 4, no. 6, pp. 391–399, Dec. 2010.
- [10] X. Wang *et al.*, "A meter-range UWB transceiver chipset for around-the-head audio streaming," in *IEEE Int. Solid-State Circuits Conf. (ISSCC) Dig. Tech. Papers*, Feb. 2012, pp. 450–452.
- [11] F. Chen *et al.*, "A 1mW 1Mb/s 7.75-to-8.25GHz chirp-UWB transceiver with low peak-power transmission and fast synchronization capability," in *IEEE Int. Solid-State Circuits Conf. (ISSCC) Dig. Tech. Papers*, Feb. 2014, pp. 162–163.
- [12] *Hearing Aid Figure Source*, accessed on Mar. 2015. [Online]. Available: <http://www.globalcaremarket.com/us/digital-behind-the-hearing-aid-factory-wholesale.html/>
- [13] Y.-H. Liu *et al.*, "A 1.9nJ/b 2.4GHz multistandard (Bluetooth Low Energy/Zigbee/IEEE802.15.6) transceiver for personal/body-area networks," in *IEEE Int. Solid-State Circuits Conf. (ISSCC) Dig. Tech. Papers*, Feb. 2013, pp. 446–447.
- [14] J. Yoo, N. Cho, and H.-J. Yoo, "Analysis of body sensor network using human body as the channel," in *Proc. ACM 3rd Int. Conf. Body Area Netw.*, Mar. 2008, Art. no. 13.
- [15] J. Yoo and H.-J. Yoo, "Emerging low energy wearable body sensor networks using patch sensors for continuous healthcare applications," in *Proc. IEEE Eng. Med. Bio. Conf. (EMBC)*, Aug. 2010, pp. 6381–6384.
- [16] A. Kara and H. L. Bertoni, "Blockage/shadowing and polarization measurements at 2.45 GHz for interference evaluation between Bluetooth and IEEE 802.11 WLAN," in *Proc. IEEE Antennas Propag. Soc. Int. Symp.*, Jul. 2011, pp. 376–379.
- [17] J. Yoo, "Is RF really an answer for healthcare applications?—Low power circuits for BAN," in *Proc. IEEE Int. Solid-State Circuits Conf. (ISSCC), Evening Panel Discussion Session 3, What Next RF Frontier?* Feb. 2012.
- [18] S. Lee, J. Yoo, and H. J. Yoo, "A 200-Mbps 0.02-nJ/b dual-mode inductive coupling transceiver for cm-range multimedia application," *IEEE Trans. Circuits Syst. I, Reg. Papers*, vol. 56, no. 5, pp. 1063–1072, May 2009.
- [19] N. Cho, J. Yoo, S.-J. Song, J. Lee, S. Jeon, and H.-J. Yoo, "The human body characteristics as a signal transmission medium for intrabody communication," *IEEE Trans. Microw. Theory Techn.*, vol. 55, no. 5, pp. 1080–1086, May 2007.
- [20] T. G. Zimmerman, "Personal area networks: Near-field intrabody communication," *IBM Syst. J.*, vol. 35, no. 3.4, pp. 609–617, 1996.
- [21] J.-C. Sun, J.-L. Chen, Y.-H. Shen, S.-C. You, S.-J. Jou, and T.-H. Sang, "A 80-uW 2-Mb/s transceiver for human body channel binaural communication," in *Proc. IEEE Biomed. Circuits Syst. (BioCAS)*, Nov. 2012, pp. 96–99.
- [22] M. D. Pereira, G. A. Alvarez-Botero, and F. R. D. Rangel, "Characterization and modeling of the capacitive HBC channel," *IEEE Trans. Instrum. Meas.*, vol. 64, no. 10, pp. 2626–2635, Oct. 2015.
- [23] M. Vallejo, J. Recas, P. G. del Valle, and J. L. Ayala, "Accurate human tissue characterization for energy-efficient wireless on-body communications," *Sensors*, vol. 13, no. 6, pp. 7546–7569, Jun. 2013.
- [24] M. Swaminathan, F. S. Cabrera, J. S. Pujol, U. Muncuk, G. Schirner, and K. R. Chowdhury, "Multi-path model and sensitivity analysis for galvanic coupled intra-body communication through layered tissue," *IEEE Trans. Biomed. Circuits Syst.*, vol. 10, no. 2, pp. 339–351, Apr. 2016.
- [25] R. Chandra and A. J. Johansson, "A link loss model for the on-body propagation channel for binaural hearing aids," *IEEE Trans. Antennas Propag.*, vol. 61, no. 12, pp. 6180–6190, Dec. 2013.
- [26] J. Bae, K. Song, H. Lee, H. Cho, and H.-J. Yoo, "A 0.24-nJ/b wireless body-area-network transceiver with scalable double-FSK modulation," *IEEE J. Solid-State Circuits*, vol. 47, no. 1, pp. 310–322, Jan. 2012.
- [27] J. Lee *et al.*, "A 60Mb/s wideband BCC transceiver with 150pJ/b RX and 31pJ/b TX for emerging wearable applications," in *IEEE Int. Solid-State Circuits Conf. (ISSCC) Dig. Tech. Papers*, Feb. 2014, pp. 498–499.
- [28] W. Saadeh, Y. Kifle, and J. Yoo, "A hybrid OFDM body coupled communication transceiver for binaural hearing aids in 65nm CMOS," in *Proc. IEEE Int. Symp. Circuits Syst. (ISCAS)*, May 2015, pp. 2620–2623.
- [29] N. Cho, L. Yan, J. Bae, and H.-J. Yoo, "A 60 kb/s–10 Mb/s adaptive frequency hopping transceiver for interference-resilient body channel communication," *IEEE J. Solid-State Circuits*, vol. 44, no. 3, pp. 708–717, Mar. 2009.
- [30] The International Commission on Non-Ionizing Radiation Protection, "Guidelines for limiting exposure to time-varying electric, magnetic, and electromagnetic fields (up to 300 GHz)," *Health Phys.*, vol. 74, no. 4, pp. 494–522, Apr. 1998.
- [31] Y. Kifle, H.-S. Kim, and J. Yoo, "Human body and head characteristics as a communication medium for body area network," in *Proc. IEEE Eng. Med. Biol. Conf. (EMBC)*, Aug. 2015, pp. 1845–1848.
- [32] J. Park, H. Garudadri, and P. P. Mercier, "Channel modeling of miniaturized battery-powered capacitive human body communication systems," *IEEE Trans. Biomed. Eng.*, to be published, doi: 10.1109/TBME.2016.2560881.
- [33] H. Cho, H. Kim, M. Kim, J. Jang, J. Bae, and H.-J. Yoo, "A 79pJ/b 80Mb/s full-duplex transceiver and a 42.5  $\mu$ W 100kb/s super-regenerative transceiver for body channel communication," in *IEEE Int. Solid-State Circuits Conf. (ISSCC) Dig. Tech. Papers*, Feb. 2015, pp. 1–3.
- [34] J. Tan and G. L. Stuber, "Frequency-domain equalization for continuous phase modulation," *IEEE Trans. Wireless Commun.*, vol. 4, no. 5, pp. 2479–2490, Sep. 2005.
- [35] D. Falconer, S. L. Ariyavisitakul, A. Benyamin-Seeyar, and B. Eidson, "Frequency domain equalization for single-carrier broadband wireless systems," *IEEE Commun. Mag.*, vol. 40, no. 4, pp. 58–66, Apr. 2002.
- [36] N. Benvenuto, R. Dinis, D. Falconer, and S. Tomasin, "Single carrier modulation with nonlinear frequency domain equalization: An idea whose time has come—Again," *Proc. IEEE*, vol. 98, no. 1, pp. 69–96, Jan. 2010.
- [37] T. Hwang, C. Yang, G. Wu, S. Li, and G. Y. Li, "OFDM and its wireless applications: A survey," *IEEE Trans. Veh. Technol.*, vol. 58, no. 4, pp. 1673–1694, May 2009.
- [38] H. Sari, G. Karam, and I. Jeanclaude, "Frequency-domain equalization of mobile radio and terrestrial broadcast channels," in *Proc. IEEE GLOBECOM*, Dec. 1994, pp. 1–5.
- [39] H. Sari, G. Karam, and I. Jeanclaude, "Transmission techniques for digital terrestrial TV broadcasting," *IEEE Commun. Mag.*, vol. 33, no. 2, pp. 100–109, Feb. 1995.
- [40] J. G. Proakis and M. Saheli, *Digital Communication*. Singapore: McGraw-Hill, 2008, pp. 95–148.
- [41] S. Haykin, *Communication Systems*. New York, NY, USA: Wiley, 2001, pp. 368–417.
- [42] K. Maharatna, E. Grass, and U. Jagdhold, "A 64-point Fourier transform chip for high-speed wireless LAN application using OFDM," *IEEE J. Solid-State Circuits*, vol. 39, no. 3, pp. 484–493, Mar. 2004.
- [43] T.-J. Kwon, J.-S. Moon, J. Sondeen, and J. Draper, "A 0.18  $\mu$ m implementation of a floating-point unit for a processing-in-memory system," in *Proc. IEEE Int. Symp. Circuits Syst. (ISCAS)*, vol. 2, May 2004, pp. 453–456.
- [44] W. H. Chen, G. Liu, B. Zdravko, and A. M. Niknejad, "A highly linear broadband CMOS LNA employing noise and distortion cancellation," *IEEE J. Solid-State Circuits*, vol. 43, no. 5, pp. 1164–1176, May 2008.
- [45] S. C. Blakmeier, E. A. M. Klumperink, D. M. W. Leenaerts, and B. Nauta, "Wideband balun-LNA with simultaneous output balancing, noise-canceling and distortion-canceling," *IEEE J. Solid-State Circuits*, vol. 43, no. 6, pp. 1341–1350, Jun. 2008.
- [46] A. D. Grasso, G. Palumbo, and S. Pennisi, "Advances in reversed nested Miller compensation," *IEEE Trans. Circuits Syst. I, Reg. Papers*, vol. 54, no. 7, pp. 1459–1470, Jul. 2007.
- [47] A. D. Grasso, D. Marano, G. Palumbo, and S. Pennisi, "Improved reversed nested Miller frequency compensation technique with voltage buffer and resistor," *IEEE Trans. Circuits Syst. II, Express Briefs*, vol. 54, no. 5, pp. 382–386, May 2007.





**Wala Saadeh** (S'12–M'16) received the B.S. degree from the Computer Engineering Department, Yarmouk University, Irbid, Jordan, in 2009, and the M.Sc. degree in microsystems engineering and the Ph.D. degree in interdisciplinary program from the Masdar Institute of Science and Technology, Abu Dhabi, United Arab Emirates, in 2012 and 2016, respectively.

From January 2013 to June 2013, she was a Test-Chip Intern at the Test-Chip Integration team, Global Foundries, Dresden, Germany, where she performed quality assurance tests on advanced nodes for the design for manufacturing. She developed a low-energy body-area-network transceiver for binaural hearing aid for long-term continuous monitoring. Since 2016, she has been with the Electrical Engineering Department, Lahore University of Management Sciences, Lahore, Pakistan, where she is currently an Assistant Professor. Her current research interests include ultralow power wearable devices, human gait analysis for elderly people, and system-on-a-chip design for portable medical devices.

Dr. Saadeh is a recipient of the IEEE International Symposium on Circuits and Systems (ISCAS) 2015 Best Paper Award (BioCAS Track) and the ISCAS 2015 Runner-Up Best Student Paper Award.



**Muhammad Awais Bin Altaf** (S'11–M'16) received the B.S. degree from the University of Engineering and Technology, Lahore, Pakistan, in 2008, and the M.Sc. and Ph.D. degrees in microsystems engineering and interdisciplinary engineering from the Masdar Institute of Science and Technology (MIST), Abu Dhabi, United Arab Emirates, in 2012 and 2016, respectively.

From 2012 to 2013, he was a Digital Design Engineer Intern at Design Solutions, Global Foundries, Dresden, Germany, where he was involved in the implementation of digital test chips in support of 20 and 14 nm technologies. In 2015, he was an exchange-Ph.D. student with the Massachusetts Institute of Technology, Cambridge, MA, USA. During his stay at MIST, he developed an energy efficient machine-learning based feature extraction and classification processor for epileptic seizure detection. Since 2016, he has been with the Electrical Engineering Department, Lahore University of Management Sciences, Lahore, where he is currently an Assistant Professor. His current research interests include physiological signal monitoring, breast cancer detection, and the development of low-power mixed-signal circuits for the portable medical applications.



**Haneen AlSuradi** (S'13) received the B.Sc. degree in electrical and electronics engineering with a minor in applied physics from the University of Sharjah, Sharjah, United Arab Emirates, in 2014, and the M.Sc. degree in electrical engineering and computer science (EECS) from the Masdar Institute of Science and Technology (MIST), Abu Dhabi, United Arab Emirates, in 2016.

She is currently a Research Engineer in Microsystems Program with the Department of EECS, MIST. Her current research interests include the modeling and fabrication of passive components on flexible substrate, including medical hydrocolloids.



**Jerald Yoo** (S'05–M'10–SM'15) received the B.S., M.S., and Ph.D. degrees from the Korea Advanced Institute of Science and Technology (KAIST), Daejeon, South Korea, in 2002, 2007, and 2010, respectively.

From 2010 to 2016, he was with the Department of Electrical Engineering and Computer Science, Masdar Institute, Abu Dhabi, United Arab Emirates, where he was an Associate Professor. Since 2017, he has been with the Department of Electrical and Computer Engineering, National University of Singapore, Singapore, where he is currently an Associate Professor. He has developed low-energy body-area-network (BAN) transceivers and wearable body sensor network using planar-fashionable circuit board for continuous health monitoring system. He has authored a book chapter in *Biomedical CMOS ICs* (Springer, 2010) and *Enabling the Internet of Things—From Circuits to Networks* (Springer, 2017). His current research interests include low-energy circuit technology for wearable bio signal sensors, flexible electronics, BAN transceivers, ASIC for piezoelectric micromachined ultrasonic transducers, and system-on-a-chip design to system realization for wearable healthcare applications.

Dr. Yoo is a recipient or a co-recipient of several awards: the IEEE International Circuits and Systems (ISCAS) 2015 Best Paper Award (BioCAS Track), the ISCAS 2015 Runner-Up Best Student Paper Award, the Masdar Institute Best Research Award in 2015, and the Asian Solid-State Circuits Conference (A-SSCC) Outstanding Design Awards in 2005. He is the Vice Chair of the IEEE Solid-State Circuits Society United Arab Emirates Chapter. Currently, he serves as a Technical Program Committee Member of the IEEE A-SSCC, the IEEE Custom Integrated Circuits Conference, and the IEEE International Solid-State Circuits Conference Student Research Preview. He is also an Analog Signal Processing Technical Committee Member of the IEEE Circuits and Systems Society.